# Numerical simulation of mixed aseismic/seismic fault-slip induced by fluid injection using coupled X-FEM analysis

Adam K. Schwartzkopff [a,*], Atsushi Sainoki [a], Derek Elsworth [b]

[a] *International Research Organization for Advanced Science and Technology, Kumamoto University, Kumamoto Prefecture, 860-8555, Japan*
[b] *Department of Energy and Mineral Engineering, G3 Centre and Energy Institute, The Pennsylvania State University, University Park, PA, 16802, USA*

ARTICLE INFO

ABSTRACT

Fluid injection into a rock mass from industrial processes can cause perceivable seismic events that may raise public concern. This seismicity can be caused by injection-induced fluid pressure in the rock mass causing slip on faults. Here we provide a method to distinguish between aseismic and seismic mobilisation and to predict fault movement due to anthropogenic fluid injection. This was achieved by extending a two-dimensional fully coupled fluid and mechanical loading extended finite element model (X-FEM) via development of a dynamic analysis module as a standalone code in MATLAB. This code considers fluid flow along the fault as well as into the rock mass and uses a directly proportional equivalent injected flow rate into the fault as the input. This model was validated by comparing the resultant pressure and normal and shear displacements calculated at the centre of the fault against observations from a decametre-scale in-situ experiment. The main results were that not only the mechanics of the fault could be simulated using this approach, but that the simulation correctly predicted the onset of seismicity and transition to dynamic analysis and at similar seismic magnitudes to observations. Parametric studies investigated the influence of the flow rate (when injecting a constant volume of water) and the effect of rate and state frictional parameters in representing modes of seismicity. The main conclusion is that this modelling technique using X-FEM provides an accurate method in accurately predicting modes, location and timing of fault remobilisation due to fluid injection inclusive of important precursory aseismic fault movements. These results are important, since they demonstrate the applicability of this X-FEM approach in accurately predicting the mechanics of fault reactivation and the resultant seismicity, aiding in the design and scheduling of fluid injection operations and in the optimisation of operational parameters.

## 1. Introduction

Fluid injection into or near a fault may induce slip and result in seismicity of sufficient magnitude to cause damage to surface and underground structures.[1–5] Fluid injection is synonymous with wastewater disposal and hydraulic fracturing used to develop sites for geothermal energy, unconventional hydrocarbon production and in destressing in deep hard rock mines. Therefore, to obtain the anticipated seismicity in geological formations, understanding the mechanics of fault reactivation is important. Understanding the resultant behaviour to fluid-injection is typically challenging due to the characteristically coupled nature of the fluid-transmission and mechanical processes. In addition, predicting the onset of seismicity, i.e., distinguishing aseismic fault movement from seismic slip, and then modelling the process under dynamic conditions remains a difficult task.

Only a few numerical methods have been utilised to model dynamic fault-slip behaviour,[6–9] still fewer have introduced numerical methods to model coupled (fluid pressure and mechanical behaviour) fault-slip behaviour[10–13] with very limited analyses representing fault-slip using coupled and dynamic analyses together.[14] The dynamic models that consider only the mechanical behaviour were conducted using the Fast Lagrangian Analysis of Continua in Three-Dimensions (FLAC3D) code, either using interface elements with the Coulomb friction law[6] or a ubiquitous joint model in order to modify the friction law used in the analysis.[7,8] The modified friction laws were Barton's[15] shear strength criterion either with or without a linear slip-weakening friction law. These studies considered fault-slip caused by the reduction in normal stress due to underground excavation. Thus, these investigations do not consider fault-slip caused by increased fluid pressure along the fault. In addition, a custom static and dynamic finite element method (FEM) code

(PyLith) was developed and implemented the Coulomb friction law, linear slip-weakening, linear time-weakening and rate and state friction with an aging law.[9] To consider fault movement resulting from fluid injection coupled numerical models are mandatory. Most of these coupled numerical models only accommodate aseismic fault-slip since they are implemented considering only static conditions[10–13] with one notable exception.[14] These coupled numerical methods involve either linking the code FLAC with a multiphase flow simulator, TOUGH,[16] or in using a custom porous medium FE model utilising interface elements[10] to further consider dynamic analysis.[14] This dynamic model only considers the static-to-dynamic transition and neglects the final dynamic-to-static transition. It is of significant importance to consider both these transitions to simulate the temporal variation of seismic activity both during and after fluid injection. In addition, although these numerical methods may provide valuable insights through parametric studies, these tools should be fully verified against laboratory and/or in-situ experiments. Additionally, there is a need to implement rate and state friction in a dynamic coupled approach. Furthermore, the potential for the fault to slip is fundamentally linked to the rate of injection relative to the permeability of the surrounding rock mass, since this controls the rate of leak-off and hence pressurisation. In order to accurately capture fault remobilisation response, some key aspects to consider include:

i. The coupling between fluid pressures and fault remobilisation is accounted for by the method, which includes fluid flow within the fault as well as leak-off into the rock mass.
ii. Appropriate rock properties can be determined and input into the model.
iii. The method is sufficiently efficient to be useful in an industrial context.
iv. The results are comparable to in-situ experiments.

Thus, the problem addressed in this study is the reproduction of the quasi-static and dynamic mechanics of a natural in-situ fault using a coupled extended finite element method (X-FEM) approach. This approach uses dynamic analysis when unstable fault-slip conditions are met (considering rate and state friction behaviour), otherwise using quasi-static analysis. Results are benchmarked against observations from a decametre-scale in situ fault remobilisation experiment.[17]

Fault-slip produced by fluid injection can be approximated by the Coulomb friction law.[1,18–22] An increase in pore pressure decreases the compressive effective normal stress along the fault, which decreases the frictional resistance. The shear stress within this pressurised region (with reduced effective stress) then produces localised frictional slip failure. Slip tendency analysis is a simplified approach for determining whether the fault will slip under the action of a given fluid pressure.[18,20] However, the slip magnitudes along the fault are more difficult to predict, since they depend on the distribution of fluid pressures along the fault and into the rock mass, the rock and fault properties and the in-situ effective stress regime.[23]

Seismic fault-slip occurs when the fault becomes unstable, i.e. when the resistance to sliding reduces more rapidly than the unloading process of the surrounding rock – thus, the surrounding rock stiffness is lower than the critical stiffness.[24] Conversely, aseismic slip occurs when the fault movement is stable, i.e. when the velocity weakening behaviour is moderate or does not occur.[17] Both aseismic and seismic slip can occur in fault systems, where seismic slip of sufficiently large energy release may pose a safety risk to structures and people.[3,17,25] For artificially perturbed fault systems, the maximum energy release (logarithmically scaled to the Richter magnitude) may be linked to both the volume and rate of fluid injection.[26]

Rate and state friction laws have been shown to accurately model representative laboratory reproduced faults using velocity step changes and hold periods.[27] Although changing the effective normal stress (due to increased fluid pressure) may change the rate and state friction

parameters,[28–30] these friction laws provide a good first approximation to represent the frictional resistance of rock faults. Another benefit of these friction laws is that they have been shown to predict the nucleation of seismicity.[24] However, under fluid pressurisation, this instability may be driven by the energy imbalance caused by a decrease in effective normal stress and in fault zone weakening, even for velocity strengthening frictional behaviour. This effect may outweigh the impact of the second order rate and state effects on the frictional strength of the fault, at least for representative laboratory reproduced fault systems.[31] As current understanding is insufficient to accurately partition between aseismic and seismic fault-slip,[32] the present study aims to gain new insights into this through X-FEM modelling using the nucleation of seismicity theory to assess when seismic fault-slip occurs, as constrained by in situ experimental observations.

The X-FEM numerical approach was originally developed to assist with crack propagation prediction[33,34] and is also applicable to the prediction of the non-linear shear behaviour of discontinuous rock resulting from fluid injection.[35] The X-FEM numerical approach was recently extended to study fractured porous media.[36–38] Our study presents an extended coupled two-dimensional X-FEM formulation[39] to consider the mechanics of fluid injection into an in-situ natural fault, with added consideration of the dynamic processes. This method is validated against an in-situ fault reactivation experiment[17] whilst examining the coupled nature of fault-slip. The validated approach contains all the necessary processes contributing to the reactivation, i.e. fluid injection, leak-off, inertial terms, and stiffness differences in the system. The method presented could be applied to other faults that are perturbed by fluid injection to forecast the expected fault movement. Inclusion of the dynamic fault-slip process in this approach provides insights into induced seismicity and may contribute to the mitigation of its risks.

## 2. X-FEM formulation for a mixed aseismic/seismic fault-slip simulation based on a coupled hydro-mechanical model

An X-FEM approach was applied since it is computationally efficient and accurate when accommodating a discontinuity, compared to conventional continuum approaches. The X-FEM modelling implicitly represents individual cracks without requiring complex meshing and remeshing of the crack, resulting in decreased computation time. Specifically, the X-FEM approach enriches the FEM model by providing additional degrees of freedom (DOF) to the nodes of the element(s) that are crossed by the discontinuity. Therefore, a single mesh can be used for discontinuities of any length and orientation.[40]

The following sections introduce the dynamic X-FEM method[39] and the model parameters used to simulate the in-situ experiment.[17] Refer to Schwartzkopff et al.[23] for the static X-FEM formulation utilised during periods of stability. A modified version of the X-FEM formulation[39] was used, incorporating reasonable assumptions, but adding the capability[23] to represent inertial (dynamic) effects. The governing equations, approximate displacement and pressure fields, and the contact model are given in Schwartzkopff et al.[23] We note that the primary contribution of the current study is the implementation of the dynamic analysis in conjunction with the switch between static and dynamic analysis.

### 2.1. Spatial discretisation of the strong formulation for X-FEM

The weak forms of the governing equations are obtained by applying the well-known divergence theorem, which are then discretised spatially, based on the Galerkin discretisation technique. The dynamic part of the analysis uses the following resulting system of linear equations, where the static analysis follows the same procedure as Schwartzkopff et al.[23]:

$$\mathbf{M}\overline{U} + \mathbf{C}\dot{\overline{U}} + \mathbf{K}\overline{U} - \mathbf{Q}\overline{P} + \mathbf{f}_U^{\text{int}} - \mathbf{f}_U^{\text{ext}} = \mathbf{0}$$

$$\mathbf{In}\overline{U} + \mathbf{Q}^T\dot{\overline{U}} + \mathbf{H}P + \mathbf{S}\dot{P} - \mathbf{q}_P^{\text{int}} - \mathbf{q}_P^{\text{ext}} = \mathbf{0} \qquad 1$$

where $\overline{U} = \langle \overline{\mathbf{u}}, \overline{\mathbf{a}} \rangle$ and $\overline{P} = \langle \overline{\mathbf{p}}, \overline{\mathbf{c}} \rangle$ are the standard and enriched degrees of freedom (DOF) of displacement and pressure, respectively. $\mathbf{M}$ is the mass matrix, $\mathbf{C}$ is the Rayleigh damping matrix, $\mathbf{K}$ is the stiffness matrix, $\mathbf{Q}$ is the coupling matrix, $\mathbf{H}$ is the permeability matrix, $\mathbf{S}$ is the compressibility matrix, $\mathbf{In}$ is the fluid inertial matrix, and $\mathbf{f}_U^{ext}$ and $\mathbf{q}_P^{ext}$ are the external force vectors. The matrices added (or redefined) compared with Schwartzkopff et al.[23] are:

$$\mathbf{M}_{\alpha\beta} = \int_{\Omega} \left(\mathbf{N}_u^{\alpha}\right)^T \rho \mathbf{N}_p^{\beta} d\Omega$$

$$\mathbf{C} = \alpha_{\text{Rayleigh}} \mathbf{M} + \beta_{\text{Rayleigh}} \mathbf{K} \qquad 2$$

$$\mathbf{In}_{\delta\beta} = \int_{\Omega} \left(\nabla \mathbf{N}_p^{\delta}\right)^T k_f \rho_f \mathbf{N}_u^{\beta} d\Omega$$

where $(\alpha,\ \beta) \in (std,\ Hev)$ represent the standard and Heaviside functions of the displacement field and $(\delta,\ \gamma) \in (std,\ abs)$ are the standard and modified level set functions of the pressure field. In these definitions, A Rayleigh damping matrix has been introduced to prevent undesirable oscillations in the dynamic system.

To assist in the approximation of the Rayleigh parameters ($\alpha_{\text{Rayleigh}}$ and $\beta_{\text{Rayleigh}}$), the natural angular frequencies are estimated, assuming a uniform rock layer on a rigid base, as[41]:

$$\omega_n = \frac{\pi(2n-1)V_s}{2h} \qquad 3$$

where $n$ is the mode number, $V_s$ is the shear wave velocity, and $h$ is the height of the layer, which was assumed to be the width of the (fault) damage zone. The shear wave velocity can be calculated as:

$$V_s = \sqrt{\frac{G}{\rho}} = \sqrt{\frac{E}{2\rho(1+\nu)}} \qquad 4$$

where $G$ is the shear modulus, and $\rho$ is the density of the medium (and $E$ is the elastic modulus and $\nu$ is the Poisson's ratio). As suggested, the first and third modes are used with a damping ratio $\xi$, which generally ranges between 2% and 5% for rock,[42] to determine the Rayleigh parameters as:

$$\alpha_{\text{Rayleigh}} = \frac{2\omega_1 \omega_3}{\omega_1 + \omega_3} \xi$$

$$\beta_{\text{Rayleigh}} = \frac{2}{\omega_1 + \omega_3} \xi \qquad 5$$

where the damping ratio was set to 4% for the dynamic analysis. Note that the modified stiffness matrix is utilised in the Rayleigh damping matrix to damp and thereby stabilise the contact tractions along the fault.

In addition, the flux vectors $\mathbf{q}_P^{int}$ that account for fluid exchange between the fault and the surrounding porous rock can be defined as[39]:

$$\mathbf{q}_{\delta}^{int} = -\int_{\Gamma_d} \left(\nabla N_p^{\delta}\right)^T \mathbf{t}_{\Gamma_d} k_{fd}(2h) \nabla p \mathbf{t}_{\Gamma_d} d\Gamma - \int_{\Gamma_d} \left(\nabla N_p^{\delta}\right)^T \mathbf{t}_{\Gamma_d} k_{fd} \rho_f(2h) \langle \ddot{\mathbf{u}} \rangle \mathbf{t}_{\Gamma_d} d\Gamma$$

$$- \int_{\Gamma_d} \left(N_p^{\delta}\right)^T \alpha_{\text{Biot}}(2h) \mathbf{t}_{\Gamma_d} \langle \nabla \dot{\mathbf{u}} \rangle \mathbf{t}_{\Gamma_d} d\Gamma - \int_{\Gamma_d} \left(N_p^{\delta}\right)^T \alpha_{\text{Biot}} [\![\dot{\mathbf{u}}]\!] \mathbf{n}_{\Gamma_d} d\Gamma \qquad 6$$

$$- \int_{\Gamma_d} \left(N_p^{\delta}\right)^T (2h) \frac{1}{K_f} \dot{p} d\Gamma + \int_{\Gamma_d} \left(\nabla N_p^{\delta}\right)^T \mathbf{t}_{\Gamma_d} k_{fd} \rho_f(2h) \mathbf{bt}_{\Gamma_d} d\Gamma + \int_{\Gamma_d} \left(N_p^{\delta}\right)^T q d\Gamma$$

Note that the hydraulic aperture $2h$ has been removed from the last integration term compared with Schwartzkopff et al.[23] since this variable can be cancelled with the flow rate defined previously.

Renshaw's[43] relationship is used to model the evolution of the hydraulic aperture as outlined and justified in Schwartzkopff et al.[23]

## 2.2. Discretisation of the time domain and solution technique

The Newmark-Beta implicit time integration scheme is utilised for the temporal discretisation of the unknown variables (of displacement and pressure), where $t_{n+1} = t_n + \Delta t$. According to this method, the acceleration $\ddot{\overline{U}}$, velocity $\dot{\overline{U}}$ and pore pressure gradient $\dot{\overline{P}}$ vectors are:

$$\ddot{\overline{U}}_{n+1} = \frac{1}{\beta\Delta t^2}\left(\overline{U}_{n+1} - \overline{U}_n\right) - \frac{1}{\beta\Delta t}\dot{\overline{U}}_n - \left(\frac{1}{2\beta}-1\right)\overline{U}_n\ddot{\overline{U}}_{n+1}$$

$$= \frac{\gamma}{\beta\Delta t}\left(\overline{U}_{n+1} - \overline{U}_n\right) - \left(\frac{\gamma}{\beta}-1\right)\dot{\overline{U}}_n - \Delta t\left(\frac{\gamma}{2\beta}-1\right)\overline{U}_n\dot{\overline{P}}_{n+1}$$

$$= \frac{1}{\theta\Delta t}\left(\overline{P}_{n+1} - \overline{P}_n\right) - \left(\frac{1}{\theta}-1\right)\dot{\overline{P}}_n \qquad 7$$

where $\overline{U}$ is the displacement vector. Note that when the model either switches to dynamic analysis, or back to static analysis, the velocity, acceleration, and pore gradient vectors are zeroed, since the model is transiting-from or -into static analysis where the material must be at rest.

Substituting then rearranging these above equations into the spatially discretised system of linear equations results in the following system of linear equations (where the iteration number is defined as $i$):

$$\begin{bmatrix} \frac{-\gamma}{\beta\Delta t}\left(\frac{1}{\beta\Delta t^2}\mathbf{M}+\frac{\gamma}{\beta\Delta t}\mathbf{C}+\mathbf{K}+\frac{\partial \mathbf{f}_U^{int}}{\partial \overline{U}}\right) & \frac{\gamma}{\beta\Delta t}\left(\mathbf{Q}-\frac{\partial \mathbf{f}_U^{int}}{\partial \overline{P}}\right) \\ \frac{1}{\beta\Delta t^2}\mathbf{In}+\frac{\gamma}{\beta\Delta t}\left(\mathbf{Q}^T-\frac{\partial \mathbf{f}_U^{int\,T}}{\partial \overline{P}}\right) & \mathbf{H}+\frac{1}{\theta\Delta t}\mathbf{S}-\frac{\partial \mathbf{q}_P^{int}}{\partial \overline{P}} \end{bmatrix}_{n+1}^{i} \begin{bmatrix} dU \\ dP \end{bmatrix}_{n+1}^{i+1}$$

$$= \begin{bmatrix} \frac{-\gamma}{\beta\Delta t}\begin{pmatrix} -\mathbf{f}_U^{int}+\mathbf{f}_U^{ext} - \left(\frac{1}{\beta\Delta t^2}\mathbf{M}\overline{U}_{n+1}+\frac{\gamma}{\beta\Delta t}\mathbf{C}\overline{U}_{n+1}+\mathbf{K}\overline{U}_{n+1}-\mathbf{Q}\overline{P}_{n+1}\right) \\ +\mathbf{M}\left(\frac{1}{\beta\Delta t^2}\overline{U}_n+\frac{1}{\beta\Delta t}\dot{\overline{U}}_n+\left(\frac{1}{2\beta}-1\right)\overline{U}_n\right) \\ +\mathbf{C}\left(\frac{\gamma}{\beta\Delta t}\overline{U}_n+\left(\frac{\gamma}{\beta}-1\right)\dot{\overline{U}}_n+\Delta t\left(\frac{\gamma}{2\beta}-1\right)\overline{U}_n\right) \end{pmatrix} \\ \mathbf{q}_P^{int}+\mathbf{q}_P^{ext} - \left(\frac{\gamma}{\beta\Delta t}\mathbf{Q}^T\overline{U}_{n+1}+\mathbf{H}\overline{P}_{n+1}+\frac{1}{\theta\Delta t}\mathbf{S}\overline{P}_{n+1}\right)+\mathbf{In}\left(\frac{1}{\beta\Delta t^2}\overline{U}_n+\frac{1}{\beta\Delta t}\dot{\overline{U}}_n+\left(\frac{1}{2\beta}-1\right)\overline{U}_n\right)+\mathbf{Q}^T\left(\frac{\gamma}{\beta\Delta t}\overline{U}_n+\left(\frac{\gamma}{\beta}-1\right)\dot{\overline{U}}+\Delta t\left(\frac{\gamma}{2\beta}-1\right)\overline{U}_n\right)+\mathbf{S}\left(\frac{1}{\theta\Delta t}\overline{P}_n+\left(\frac{1}{\theta}-1\right)\dot{\overline{P}}_n\right) \end{bmatrix}_{n+1}^{i}$$

$$8$$

where the Jacobian (first matrix of Eq. (8)) was made semi-symmetrical (except for the fluid inertial matrix **In**, which can be omitted, if required) by multiplying the first row by $-\gamma/\beta\Delta t$ to reduce the computational cost.

This defines the full suite of terms contributing to the Jacobian. Note that the Newton-Raphson iterative method is used to reduce the error to within a predefined tolerance - in this case <1% in each time step.

### 2.3. Frictional model

To capture changes in the friction coefficient from the evolution of slip velocity and healing rate, a modified version of the Coulomb friction law using rate and state parameters is implemented in the X-FEM model.[44] For cohesionless frictional faults, the original Coulomb friction law can be expressed simply as:

$$|\tau| = \mu\sigma_n' \qquad 9$$

where $\tau$ is the shear stress that is present at a location along the fault, $\sigma_n'$ is the effective normal compressive stress, and $\mu$ is the friction coefficient. The frictional coefficient can vary over the length of the fault. The effective normal compressive stress is simply the normal compressive stress minus the fluid pressure along the fault – assuming a Biot coefficient $\alpha_{Biot}$ of unity. Note that if the effective normal compressive stress becomes tensile, when the fluid pressure is greater than the normal compressive stress, the shear stress and strength reduce to zero and this point along the fault must slip, since the fault is then considered open. Hence, this friction law determines under what stress conditions a fault surface will slip. Rate state friction relates the friction coefficient to the rate of tangential shear displacement and the duration at that state.[27] The Dieterich (aging) constitutive law, used here to simulate dynamic frictional response, can be expressed as:

$$\mu = \mu_0 + a\ln\left(\frac{V}{V_0}\right) + b\ln\left(\frac{V_0\theta}{D_c}\right) \text{ and } \frac{d\theta}{dt} = 1 - \frac{V\theta}{D_c} \qquad 10$$

where $\mu_0$ is the residual friction coefficient, $a$ is an empirical dimensionless coefficient which controls the velocity response, $V$ is the tangential velocity, and $V_0$ is a reference velocity. The parameter $b$ is an empirical dimensionless coefficient that controls the state response, $D_c$ has been interpreted as the slip required to renew surface contacts and $\theta$ is the contact time parameter. This constitutive law provides a relationship that captures the time and velocity dependence of friction. Noting the difference between Schwartzkopff et al.[23] and this study is that the parameter $b$ is set as non-zero (positive).

To account for the static frictional response, i.e. the degradation of the friction coefficient with the change in shear displacement from initial in-situ conditions ($\Delta u_s$), the residual friction coefficient ($\mu_0$) is reduced linearly over a critical slip weakening distance ($Slip_c$) from an initial value ($\mu_i$) to a final value ($\mu_f$), i.e.:

$$\mu_0 = \begin{cases} \mu_i - (\mu_i - \mu_f)\dfrac{|\Delta u_s|}{Slip_c} \text{ if } |\Delta u_s| < Slip_c \\ \mu_f \text{ if } |\Delta u_s| \geq Slip_c \end{cases} \qquad 11$$

### 2.4. Conditions for dynamic analysis

The analysis is transferred into dynamic mode when the following instability condition is met[24]:

$$\frac{GD_c}{(b-a)} < -\sigma_n'L \qquad 12$$

where the shear modulus $G$ is of the rock surrounding the fault, $L$ is the continuous slipping area of the velocity weakening region and the other parameters are as defined earlier. Noting that the effective normal stress is the weighted average along the velocity weakening slipping area (and negative values are in compression, in this study), and if the parameter $b$

is variable it is also the weighted average of the velocity weakening zone. Note that the geometric constant is assumed to be unity, and therefore not explicitly shown in the above expression. This criterion is checked for every continuous velocity weakening area.

When the mean tangential shear-slip acceleration becomes negative, i.e. when deceleration occurs along the fault, the dynamic analysis is transferred to static analysis. That is, deceleration in fault-slip is used as a criterion to cease the dynamic analysis. In fact, when deceleration occurs, the number of fault patches undergoing slip reduces due to the increase in frictional resistance. Thus, under such conditions, dynamic analysis is not required.

## 3. Verification of the X-FEM code

The aforementioned model is used to represent fault reactivation during a well-constrained field experiment.[17] See Schwartzkopff et al.[23] for a short description of the in-situ experiment, the numerical model setup, and boundary and analysis conditions used. Note that the time increment ($\Delta t$) for the dynamic analysis was determined to be $1 \times 10^{-4}$ s.

### 3.1. Flow rate input and associated assumptions

To convert the flow rate from the in-situ experiment that would flow through multiple fractures in the 1.5 m pressurised section to a single representative fracture, the flow rate was divided by the number of fractures (NoF) that would have been encountered in the in-situ experiment. As with Schwartzkopff et al.,[23] it was estimated that there were $83 \pm 37$ fractures in the 1.5 m pressurised zone, based on 10 fracture density values from previous studies on faults transecting carbonates. The pressure increase at the injection section would therefore flow into multiple discontinuities. The following expression is the conversion in flow rates between all the fractures to a single fracture, which is used as direct input into the simulation ($q$ in Eq. (6)):

$$\text{flow rate}_{\text{one fracture}} = \frac{\text{flow rate}_{\text{all}}}{\text{NoF}} \qquad 13$$

Note that this definition differs from Schwartzkopff et al.[23] since the hydraulic aperture $2h$ is removed from the last integration term of Eq. (6). Hence, one strong discontinuity is used to represent the in-situ fault. As with Schwartzkopff et al.,[23] the assumption of using one strong discontinuity is valid since the apparent normal and tangential stiffnesses are used for the calculation of the normal and shear displacements during the simulation - a common assumption.[45–48] See Schwartzkopff et al.[23] for a discussion on how the number of fractures influences the range of related input values and that the range used for each input value is larger than the effect of changing the number of fractures from 83 to the upper bound (120 fractures) or lower bound (46 fractures).

### 3.2. Verification using PEST software

History matching was used to verify the dynamic X-FEM code. History matching is a type of inverse problem in which the observations in the reservoir (pressures and displacements in the present study) are used to estimate model variables that caused that response. The process implies that the input parameters have some physical interpretation and optimises these variables to reproduce the observed measurements (that is, in the present study, from the in-situ experiment). These problems are usually ill-posed with many parameter combinations that result in equally good matches to the past observations.[49] See Schwartzkopff et al.[23] for a discussion on previous uses of the PEST software suite in the literature.

**Table 1**
Parameters for the uncalibrated dynamic case (taken from the calibrated static case) and calibrated dynamic case.

| Parameter | Uncalibrated dynamic case (taken from the calibrated static case) | Calibrated dynamic case |
|---|---|---|
| Damage zone elastic modulus $E$ (GPa) | 16.2 | 16.2 |
| Damage zone Poisson's ratio $\nu$ | 0.34 | 0.34 |
| Intact zone elastic modulus $E$ (GPa) | 29.2 | 29.2 |
| Intact zone Poisson's ratio $\nu$ | 0.33 | 0.33 |
| Density $\rho_s$ (kg/m$^3$) | 2364 | 2364 |
| Porosity $n$ (%) | 14.25 | 14.25 |
| Fault damage zone permeability $k_f$ (m$^2$) | $4.93 \times 10^{-14}$ | $1.40 \times 10^{-13}$ |
| Biot poroelastic constant $\alpha_{\mathrm{Biot}}$ | 0.77 | 0.78 |
| Initial hydraulic aperture $2h_0$ (m) | $4.79 \times 10^{-5}$ | $4.71 \times 10^{-5}$ |
| Kappa factor $\kappa$ | 1.2 | 1.2 |
| Apparent normal stiffness $\overline{k}_N$ (GPa/m) | 27.7 | 28.0 |
| Apparent tangential stiffness $\overline{k}_T$ (GPa/m) | 11.5 | 12.5 |
| Dilation angle $\varphi_d$ (°) | 19 | 19 |
| Initial frictional coefficient $\mu_i$ | 0.68 | 0.95 |
| Final frictional coefficient $\mu_f$ | | 0.80 |
| Critical slip weakening distance $Slip_c$ (m) | Not applicable | $1.0 \times 10^{-3}$ |
| $a$ parameter | $2.69 \times 10^{-2}$ | $2.70 \times 10^{-2}$ |
| $b$ parameter | $3.69 \times 10^{-2}$ | $3.70 \times 10^{-2}$ |
| $D_c$ (m) | $2.00 \times 10^{-5}$ | $2.14 \times 10^{-5}$ |
| Reference velocity $V_O$ (m/s) | $1.0 \times 10^{-7}$ | $8.4 \times 10^{-8}$ |
| Number of fractures | 83 | 83 |
| Standard deviation of non-logarithmised fracture asperity heights $\sigma_h$ (m) | $1.9 \times 10^{-4}$ | $2.0 \times 10^{-4}$ |

### 3.3. Verification result

#### 3.3.1. Calibration of input parameters using the PEST software

The Levenberg-Marquardt algorithm[50] is used in PEST to reduce the objective function, which is the summation of the squared weighted residuals. The smaller the objective function the closer the overall fit to the measurements. By using the parameters from the calibrated static case (see Table 1), the initial weighted objective function was 49.03, with individual contributions from the pressure, shear displacement and normal displacement measurement groups of 1.10, 40.56, and 7.37, respectively. This corresponded to a coefficient of determination ($R^2$) of 0.5990 and a ratio of 0.8266 between the normalised measured data and normalised modelled values (which corresponds to an overestimation). The observation measurements of the pressure, and shear and normal displacements for every 5 s were given weightings of 0.2565, 0.8570, and 1.1464, respectively. These weightings alter the total objective function to reflect the measured magnitudes and this results in an unbiased weighted objective function. See Schwartzkopff et al.[23] for how these weightings were calculated. The observation measurements and the modelled values were linearly interpolated from the published data and the simulations, to obtain values for every 5 s up to 1400 s.

The other parameters required for the simulation were kept constant for each case, as defined in Schwartzkopff et al.[23]

The PEST calibration process reduced this initial objective function to 14.33 (approximately 29.2% of the initial weighted objective function), with individual contributions from the pressure, shear displacement and normal displacement of 3.13, 8.79, and 2.41, respectively (using the same weightings for each observation group). Using the calibrated parameters, the $R^2$ value was 0.8502 with a ratio of 1.0042 between the normalised measured data and the normalised model

values (corresponding to a slight underestimation) and representing a good match.

#### 3.3.2. Simulation result with calibrated parameters

Fig. 1 illustrates the results using the calibrated values, for both the mixed dynamic/static simulation and the static only simulation, compared to the measured in-situ data. This shows that after initial slip using dynamic analysis the pressure decreases compared to the static only simulation. The shear displacement history is similar using the mixed dynamic/static analysis compared with static only analysis, with the major difference being the last slip event in the mixed dynamic/static analysis. This slip event from about 1320 s to 1400 s follows the overall trend of the in-situ experimental data. This slip event also increases the normal displacement during this time period, due to dilation. Noting that because of the slightly higher initial slip there is more opening displacement with the mixed dynamic/static analysis, which is closer to the in-situ experimental data. This would explain the lower pressure at the injection point since the hydraulic aperture is greater in the mixed dynamic/static analysis. In general, by using the mixed dynamic/static analysis the results are in closer agreement with the pressure and displacement data, recorded in the in-situ experiment. It is therefore important to perform mixed dynamic/static analysis to reproduce the complex mechanical behaviour of the fault and pore pressure change that cannot be fully captured with the static only analysis. The mixed dynamic/static analysis took approximately 18,651 s (5 h, 10 min, and 51 s), whereas the static only simulation took 8,478 s (2 h, 21 min, and 18 s) to complete. Although the mixed dynamic/static analysis takes about 2.2 times longer than the static analysis it adds important features of the fault reactivation process, as well as possibly distinguishing between aseismic and seismic fault slip. Therefore the remainder of the discussion is related to the mixed dynamic/static simulation.

As shown in Fig. 1 (a), the variation in pressure with time at the injection point follows the measured data very well and on average is 0.19 MPa lower than the measured values. The final fluid pressure value at 1400 s was 3.70 MPa, which was close to the measured value at 1400 s of 3.42 MPa. The simulated fluid pressure at the injection point pressurised up until about 920 s then remained fairly steady for the rest of the simulation, until 1400 s. That is, the pressure versus time simulated values shows a similar trend to the experimental pressure data.

The simulated values of shear displacement versus time follow a similar trend to the experimental data and is on average 0.06 mm higher than the measured values, as shown in Fig. 1 (b). That is, the fault experiences slip at about 900 s then stops, after which at about 1320 s there is a second slip event in the simulation, which is about 120 s later than that recorded in the experiment. The final simulated shear displacement at 1400 s was 0.88 mm, which is comparable to the measured value of 1.17 mm.

The simulated values of normal displacement versus time also follow a similar trend to the experimental data and is on overage 0.05 mm lower than the measured values, as shown in Fig. 1 (c). Up until 900 s from the start of fluid injection the difference between the measured and modelled values are negligible. Then after about 900 s, as a result of dilation, the fault opens at the injection point then stops, then when the fault experiences a second slip event the fault opens more, then remains fairly stable for the rest of the simulation. The final simulated opening displacement value at the injection point was 0.45 mm, which is close to the measured value of 0.64 mm.

Fig. 2 shows the total displacement field from in-situ conditions at approximately 1400 s into the simulation, which demonstrates that the movement induced from fluid injection is concentrated around the injection point (at the centre of the model).

Fig. 3 shows the change in pore pressure field from in-situ conditions at approximately 1400 s into the simulation, illustrating that the pore pressure is concentrated around the fluid injection point (at the centre of the model).
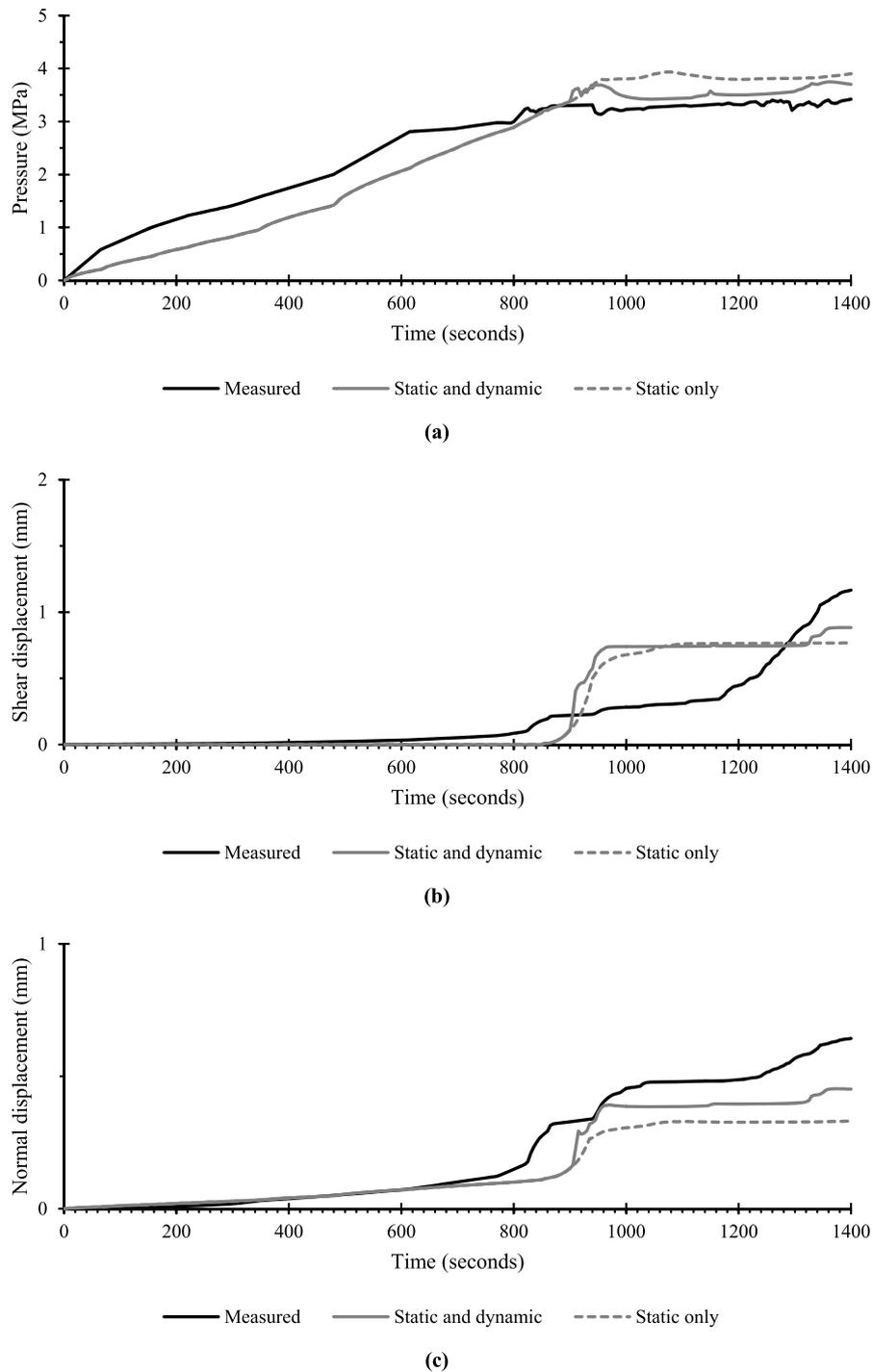
**Fig. 1.** **(a)** Pressure, **(b)** shear displacement, and **(c)** normal displacement at the injection point over time for the calibrated dynamic and static simulations.

Fig. 4 (a) shows the pressure history along the fault, illustrating the pressure increase and the diffusion of fluid away from the injection point, Note that the positive values from the injection point are deeper along the fault. The zone of fluid pressure >1 MPa at approximately 1400 s ranges between approximately −60 m–80 m from the injection point (140 m in total), which illustrates that the fluid pressure preferentially was transferred deeper along the fault compared to up the fault, because of gravity. The pressure history is smooth with notable increases at 930 s, 1135 s, and 1325 s.

The shear displacement history along the fault, as shown in Fig. 4 (b), is smooth until approximately 930 s. Following this, when the fault becomes tensile at one section, below the injection point, the shear displacement splits into two peaks away from this section. The shear displacement area at 1400 s ranges from approximately −40 m–50 m from the injection point, which shows that the shear displacement area follows the increased pressurised area.

Similar to the shear displacement history along the fault, the normal displacement history along the fault, as shown in Fig. 4 (c), is smooth until approximately 930 s. After this time, one section of the fault just below the injection point becomes tensile (i.e. the fault surfaces are no longer in contact). This results in this section of the fault not being influenced by the dilation from shear movement. The section where
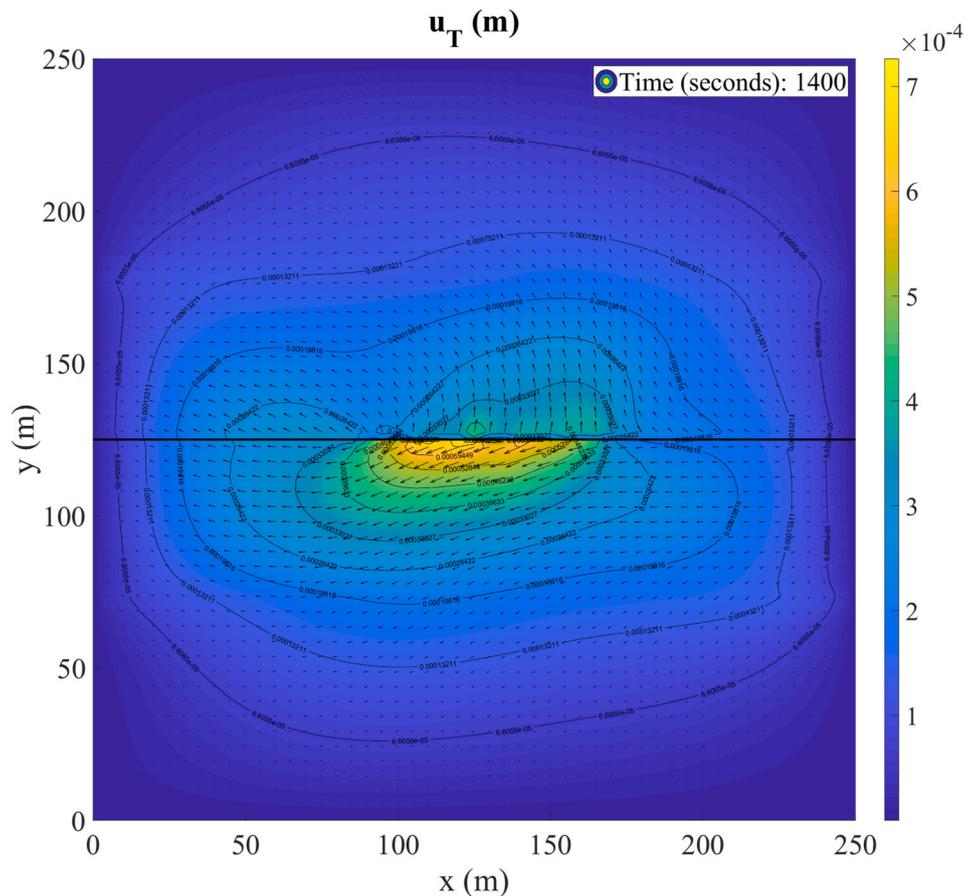
**Fig. 2.** Total displacement field at approximately 1400 s.

normal displacement is increased (above about 0.1 mm) at 1400 s ranges from approximately −40 m–50 m, which illustrates that this normal displacement range is influenced by the increased pressurised area.

### 3.3.3. Model verification in terms of aseismic-to-seismic slip ratio

The dynamic analysis was used when the instability criterion was met (Eq. (12)). This resulted in four distinct seismic periods (see Fig. 5). The first seismic period where dynamic analysis was used was at ~900 s into the simulation, after shear slip had initiated, and lasted for ~55 s. Interestingly, the next major seismic period was calculated to be at 1110 s into the simulation, which is similar to the measured start of seismicity at 1100 s in the in-situ experiment. This dynamic period went from 1110 s to 1160 s in the simulation (a period of 50 s). The in-situ experiment measured half the seismic events from 1000 s to 1190 s. There were one other seismic periods in the simulation after the main seismic period, at 1285 s (lasting ~70 s). Noting that if a static analysis time step was bounded by two dynamic analysis periods, this static analysis time step is grouped as the same seismic period.

Fig. 6 illustrates that the dynamic analysis is able to capture high velocities in the simulation, in this case at 1295.73 s after the start of injection the maximum velocity simulated is just above 0.047 m/s. In this case there are two high velocity zones, both above and below (and close to) the injection point.

The ratio of dynamic shear movement to total shear movement was 1.10%. The dynamic shear movement to total shear movement was calculated by the absolute cumulative weighted average shear movement along the fault during the dynamic analysis and compared to the total absolute cumulative weighted average shear movement along the fault. This is a reasonable value since other numerical results using rate and state friction state reported this ratio was approximately 1% for low amounts of seismic activity, with seismic magnitude ~0.3 [51]. In

addition, it has been shown that most (>95%) of the deformation induced by fluid injection is aseismic, during in-situ experiments, at the scale of tens of metres,[52–55] in the laboratory[56] and during reservoir stimulations.[57,58]

The seismic moment was calculated at every time step:

$$M_0 = G|\Delta u_s|A \qquad 14$$

where $G$ is the shear modulus, $|\Delta u_s|$ is the absolute weighted shear displacement change from in-situ conditions for the slipping area $A$. The seismic magnitude can be approximated from the seismic moment using the following expression[59]:

$$M_w = \frac{2}{3}\log_{10}(M_0) - 6.0 \qquad 15$$

The ratio of dynamic shear movement to total shear movement (1.10%) is multiplied by the seismic moment to approximate the dynamic seismic magnitude (see Fig. 7). Interestingly, the average dynamic seismic magnitude for the dynamic periods was −2.002, which is in agreement with the calculated value of approximately below −2 for the in-situ experiment. Demonstrating that, as with the in-situ experiment, the slip was mostly aseismic in the simulation.

The ratio of dynamic shear movement to total shear movement for each point along the fault during the simulation is shown in Fig. 8. This illustrates that the majority of the seismic shear movement was remote from the injection point and near the shear stress fronts. This is in agreement with many studies on induced seismicity due to fluid injection.[17,29,60] More seismic shear movement occurred below the injection point at the shear stress front (downwards in the direction of gravity).

**Pore pressure change (MPa)**
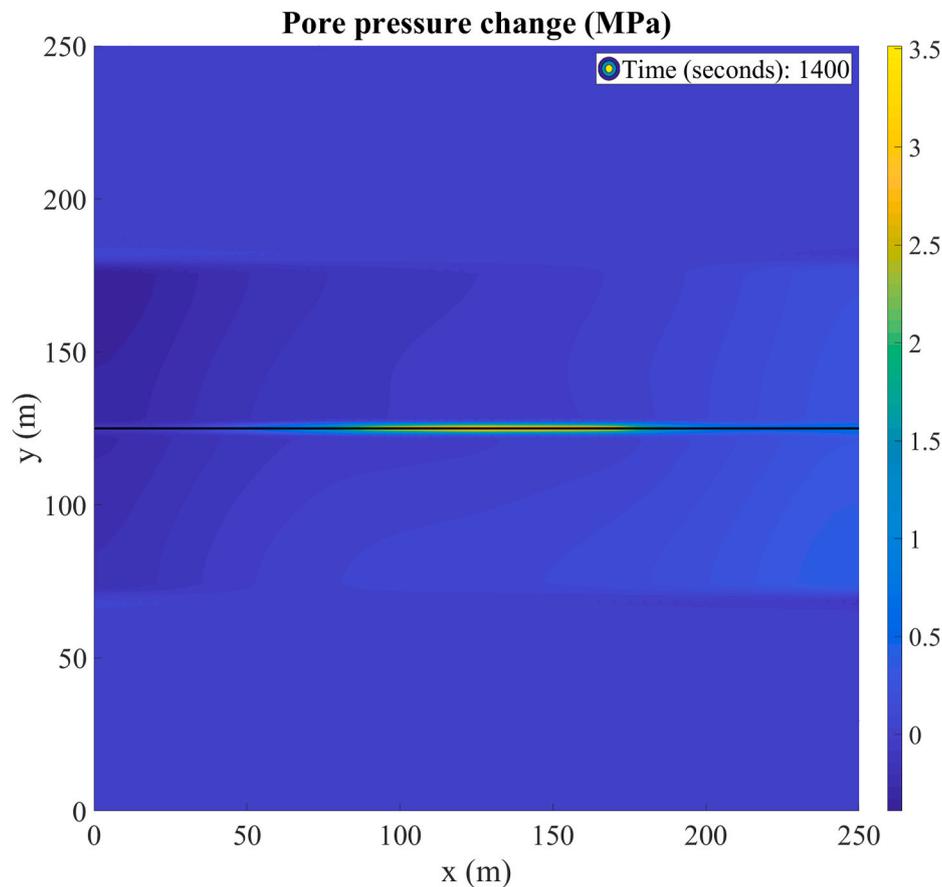


**Fig. 3.** Change in pore pressure field from in-situ conditions at approximately 1400 s.

## 4. Parametric investigations into the seismicity produced from fluid injection

Two parametric studies were conducted to investigate the role of the injection rate and the *b* parameter (which controls the amount of decrease in the friction coefficient) on the seismicity produced. Since the volume of fluid to be injected is normally predetermined, it is important to understand what injection rate the operation should use to mitigate damaging seismicity. The *b* parameter is an important controlling factor in the nucleation of seismicity. Investigating changes in the *b* parameter (within a reasonable range) illustrates how this X-FEM model can quantify the risk due to uncertainty in parameters. These parametric studies aim to clarify the seismic response due to injecting a constant volume under different conditions to assist in the understanding and hence possible mitigation of seismicity. The first focussed on injecting 1 cubic m of water into the same configuration using different constant flow rates (from $4 \times 10^{-4}$ cubic m per s to $4 \times 10^{-3}$ cubic m per s). The second investigated the influence of the *b* parameter on the level of seismicity predicted by the simulations, using the flow rate that produced the greatest seismicity by injecting 1 cubic m of water into this fault. The material and fault properties obtained from calibration were used in these studies.

### 4.1. The influence of the injection rates on the aseismic and seismic fault-slip injecting a constant volume into the fault

By increasing the flow rate but maintaining a constant injection volume (i.e. by changing the injection period during the simulation) results in the pressure at the injection point increasing more rapidly with the cumulative injected volume as well as producing an overall higher pressure during the simulation, referring to Fig. 9 (a). This results in the

fault slipping earlier and more initially, as shown in Fig. 9 (b). Increasing the flow rate generally produces more shear displacement in the simulation, with the exception of the $1 \times 10^{-3}$ cubic metres per s simulation, since the frictional model is complex owing to its dependency on the slipping velocity and contact time. Note that Fig. 9 (b) includes both seismic and aseismic fault-slip. In the pressurisation stage (without slipping taking place), the normal displacement increases faster with the cumulative injected volume. After the fault slips, the normal displacement increases because of the dilation. The normal displacement for these models increases with increasing flow rate, except for the flow rate of $8 \times 10^{-4}$ cubic m per s since when the fault is in contact (the pressure is below the initial effective normal stress), the fault slips less compared with the other selected simulations, producing a lower overall normal displacement (see Fig. 9 (c)). Note that dilation affects the normal displacement around the injection point, which would influence the normal displacement magnitude at the injection point as well.

Fig. 10 shows a summary of the pressure, shear displacement and normal displacement at the end of the simulations for different flow rates (injecting a total of 1 cubic m of water into the fault). The final simulated pressure increases approximately linearly from 3.83 MPa for the $4 \times 10^{-4}$ cubic m per s flow rate to 5.28 MPa for the $4 \times 10^{-3}$ cubic m per s flow rate. This results in the final shear displacement values in general increasing when raising the flow rate. As there is a complex non-linear relationship between the pressurisation rates and hence the slipping rate and friction coefficient, this produces a scattered relationship between flow rate and final shear displacement at the injection point. However, in general the higher the flow rate, the greater the pressure and then the shear displacement increases. The final normal displacement at the injection point is fairly constant, when varying the flow rate, at about 0.4 mm. The minimum and maximum slipping pressure values are calculated from the final and initial friction coefficients,

**(a)**



**(b)**



**(c)**
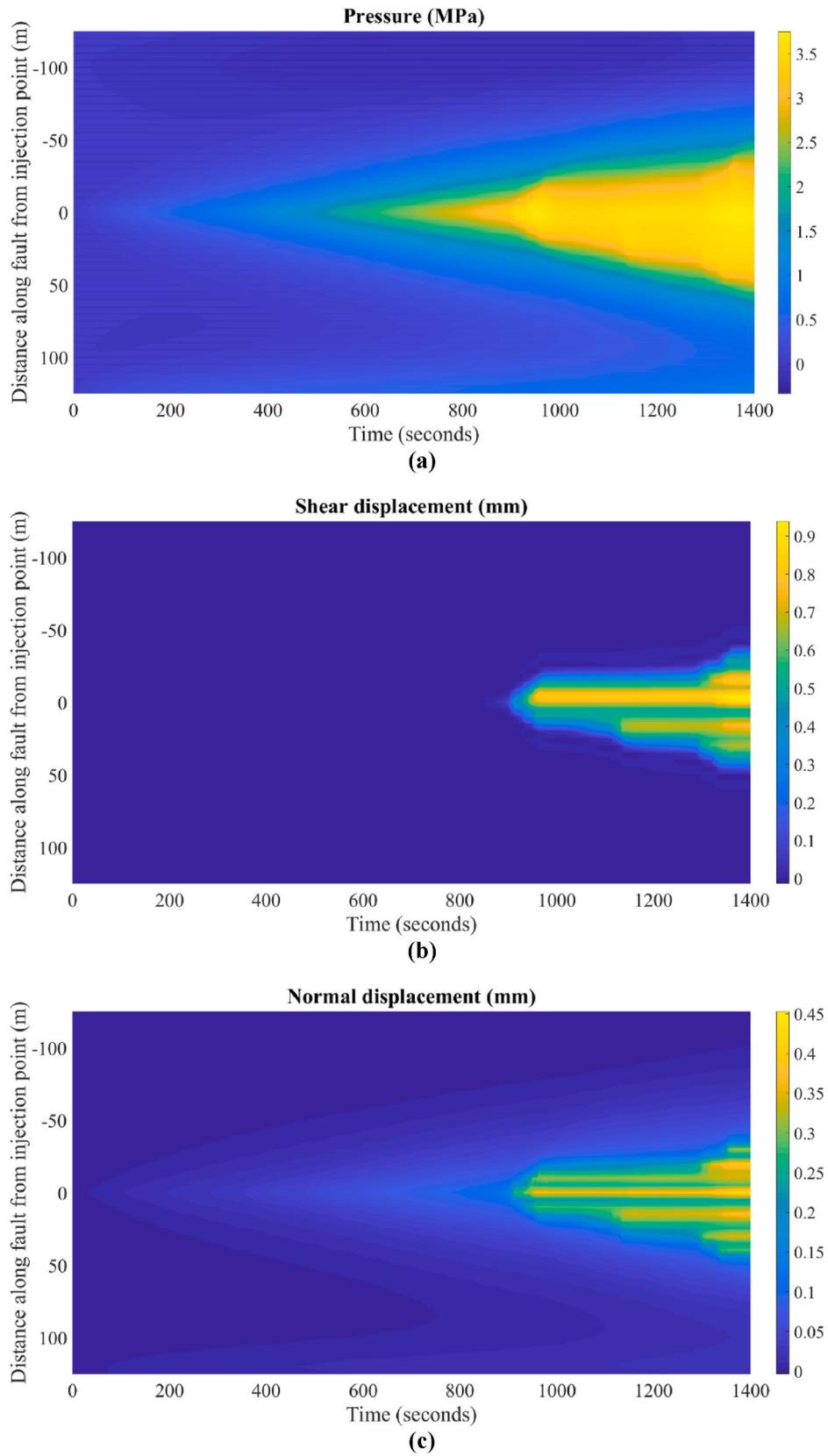
**Fig. 4. (a)** Pressure, **(b)** shear displacement, and **(c)** normal displacement along the fault over time for the calibrated simulation.
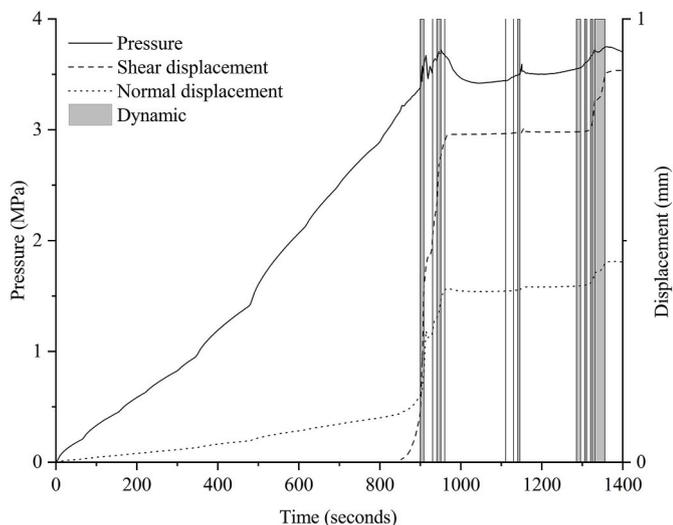
**Fig. 5.** Simulated pressure, shear displacement and normal displacement over time at the injection point, showing the dynamic periods (noting that these dynamic periods include some static time steps that are bounded by dynamic periods for graphing purposes).

respectively, and do not take into account the rate and state friction effects.

Fig. 11 shows the same final pressure values and the seismic to total slip ratio with respect to the flow rate (injecting a constant volume of 1 cubic m). When the final pressure value falls within a range from the maximum slipping pressure to the initial effective normal stress, the

fault surfaces are in contact and fault-slip is occurring. Since this maximises the amount of the slipping area that is in contact, this produces the greatest amount of seismicity, indicated by the seismic to total slip ratio. When the pressure is below or close to the maximum slipping pressure, this produces less seismicity since there is less slipping area (that is in contact). As the injection rate increases, it reduces the simulated seismicity, since the centre of the fault becomes tensile and separates and these areas that are not in contact will not contribute to indicating seismic events, because of the instability theory used, see Eq. (12). Therefore, increasing the flow rate may contribute to reducing the severity of seismicity, however, as the pressure at the injection point becomes higher, it has the possibility of inducing tensile fractures into the rock mass and/or causing fault propagation. If seismic fault-slip can be accurately estimated (using methods such as the one presented), there is a possibility of allowing large aseismic fault-slip events to occur while minimising the seismic fault-slip (considering a threshold of allowable seismicity). By understanding the conditions and magnitudes of seismicity caused by fluid injection, this may assist in determining fluid injection protocols for industry. This may give greater confidence and control to operations such as for shale gas recovery, enhanced geothermal systems, and wastewater disposal.

The amount of seismicity will change dependent on the properties of the rock mass and the fault. Therefore, careful consideration of these properties must be taken into account, with one of the most important and influential parameters being the friction coefficient of the fault core. In addition, estimating the pressurisation history, from determining the fault permeability and damage zone permeability, is important to determine the maximum pressure from a corresponding injection scheme.
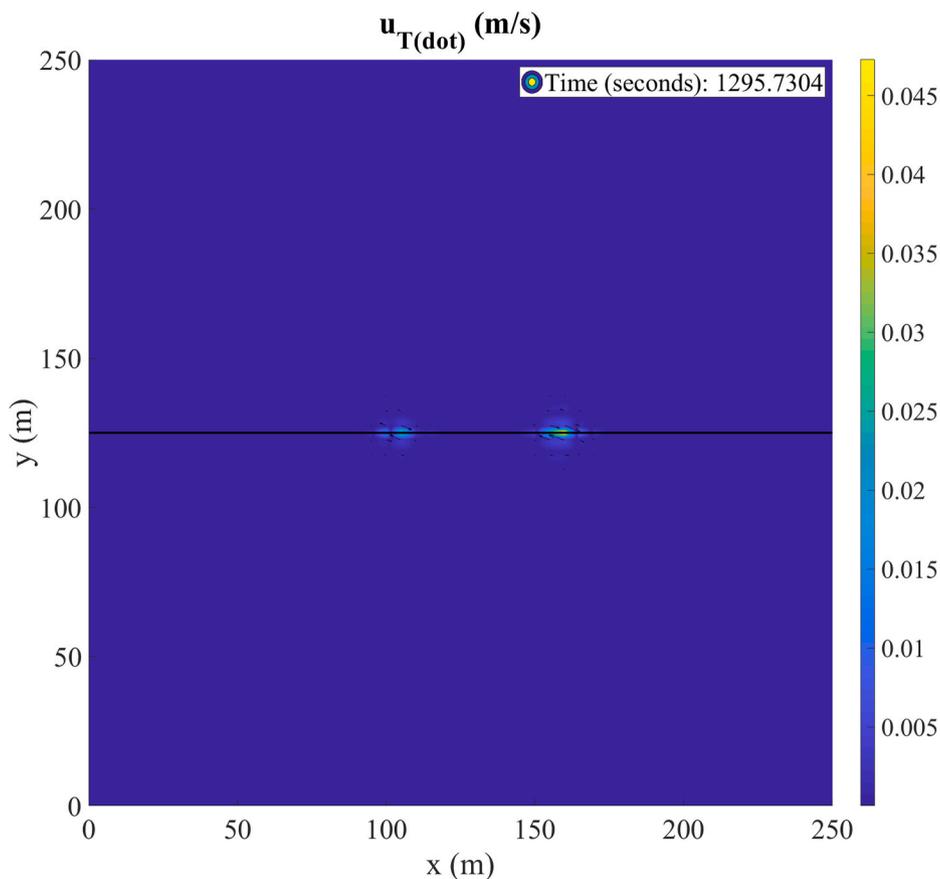


**Fig. 6.** An example of the total velocity field during dynamic analysis, showing a maximum velocity of approximately 0.047 m/s.
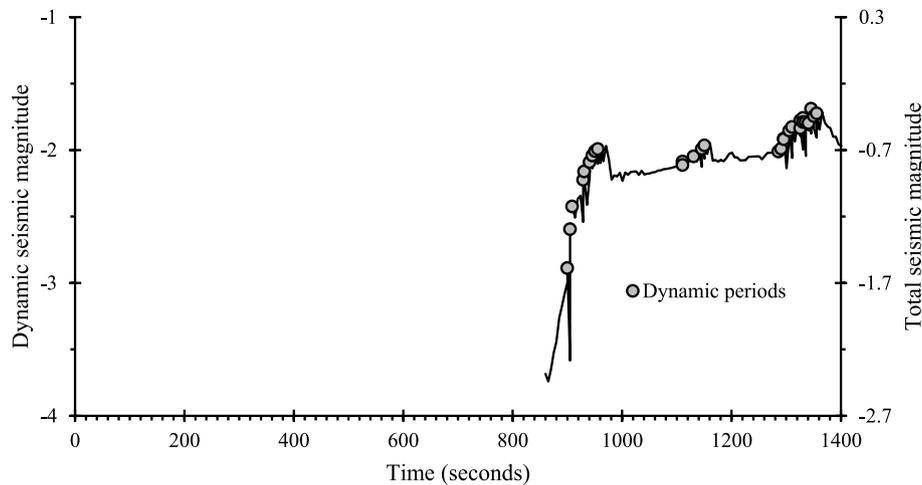
**Fig. 7.** Simulated dynamic and total seismic magnitudes over time, showing the dynamic periods.
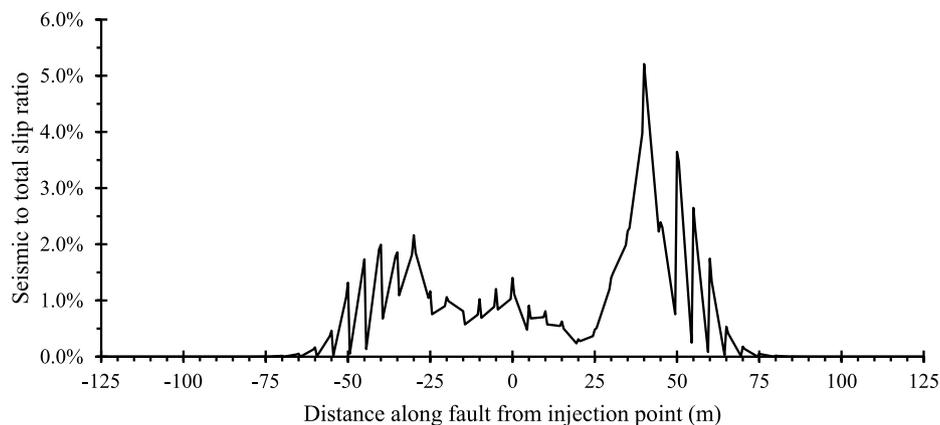


**Fig. 8.** Simulated seismic to total slip ratio along the fault.

*4.2. The influence of (b-a) values on the aseismic and seismic fault-slip injecting a constant volume at a constant flow rate*

Taking the injection rate that produces the maximum seismic to total slip ratio from the previous simulations ($6 \times 10^{-4}$ cubic m per s), another parametric study was conducted to investigate the influence of the *b* parameter on the predicted seismicity using the same rock mass and fault properties of the calibrated simulation.

Fig. 12 shows the pressures, shear displacements and normal displacements at the injection point from the end of each simulation, by changing the *b* parameter from equal to the *a* parameter to 0.025 more than the *a* parameter (in 0.005 increments). The final pressure simulated decreases with increasing the *b* parameter. At low *b* parameter values, therefore the pressure is higher, thus producing more slip for the (*b-a*) value equal to 0 and 0.005. The shear displacement then decreases because of the lower pressures experienced, before increasing with the increasing *b* parameter, since the higher the *b* parameter the greater reduction in the frictional coefficient when slip occurs, promoting more fault-slip. The normal displacement values are affected by both the pressure and the amount of shear displacement. As the pressure decreases so does the opening however, as the shear displacement increases so does the normal displacement due to dilation. This produces a minimum normal displacement at (*b-a*) value of 0.02, since the pressure is still relatively low compared to the other simulations and this

simulation produces less shear displacement than the (*b-a*) value of 0.025, which opens the fault due to dilation.

According to the conditions for dynamic analysis (see Section 2.4) a velocity neutral fault will not produce any seismicity, resulting in a seismic to total slip ratio of zero for the (*b-a*) value of zero. From the (*b-a*) value of 0.005–0.025 the amount of seismicity seems to scale approximately linearly with the (*b-a*) value, reaching a maximum of about 4.2% at the (*b-a*) value of 0.025, see Fig. 13. Therefore the (*b-a*) value effects the amount of seismic to total slip ratio proportionally. This indicates the importance of measuring or estimating the rate and state frictional parameters for a fault. The residual frictional coefficient and the *a* and *b* parameters would vary spatially along the fault core. This demonstrates the importance of estimating or measuring these local frictional parameters at the injection site.

## 5. Advantages of the coupled X-FEM approach to quantify mixed aseismic/seismic fault-slip

It is important to be able to predict when seismic fault-slip occurs and the seismic magnitude produced.[51] Seismic fault-slip may cause unwanted damage to surface and underground structures if the seismic magnitude is high enough.[1–5] Conversely, aseismic slip will not radiate seismicity however, may cause fault propagation.[61] Therefore, there may be a method to optimise fluid flow based on a concept that attempts

(a)



(b)



(c)
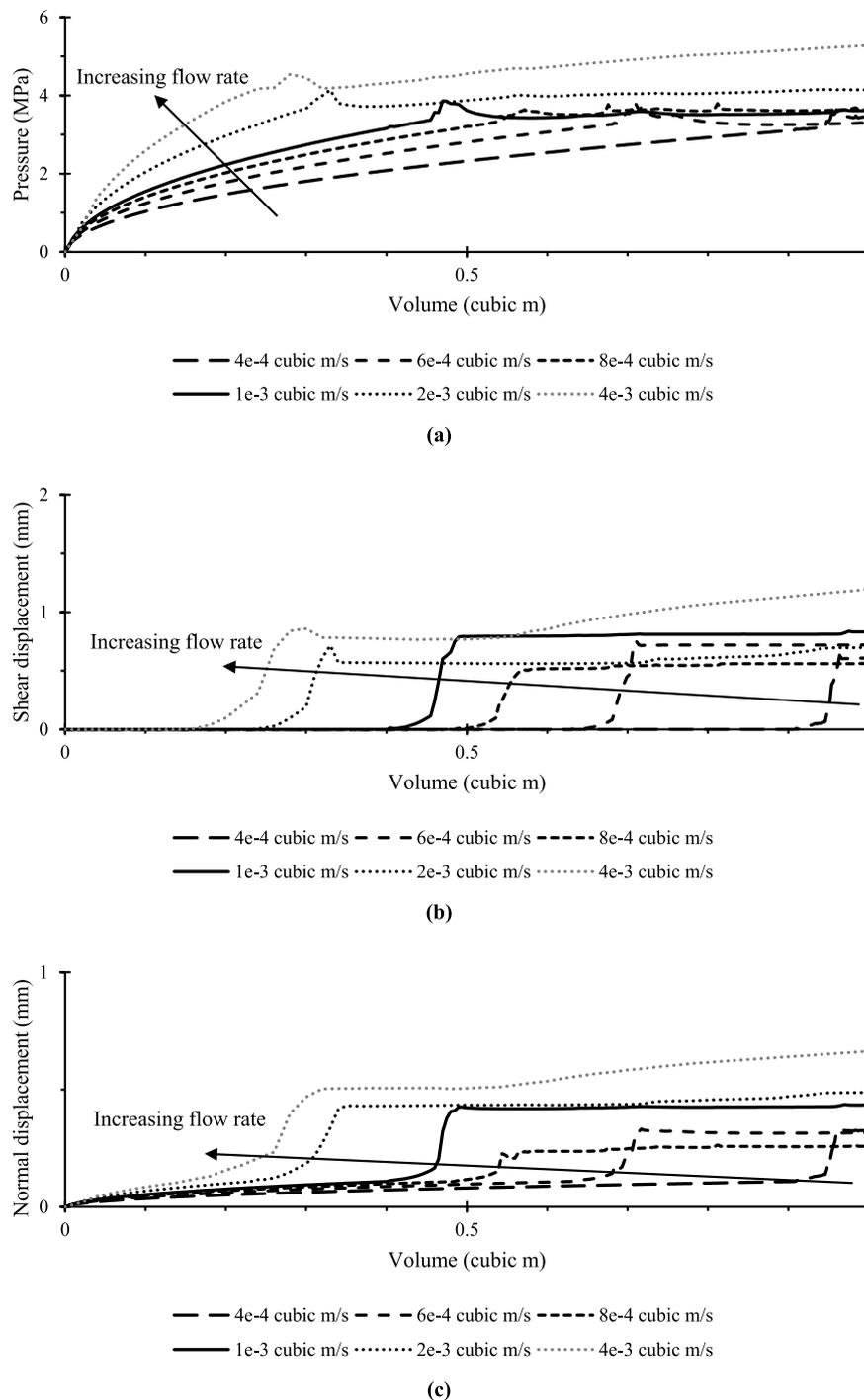
**Fig. 9.** **(a)** Pressure, **(b)** shear displacement, and **(c)** normal displacement at the injection point versus cumulative injected volume at selected flow rates.

to minimise the seismic magnitude. In such a method, aseismic fault-slip could occur if it cause neither rock failure nor fault rupture. In addition, if seismic fault-slip can be properly predicted and partitioned from the aseismic fault-slip, it would be possible to estimate the severity of ground vibration accurately. This would assist with mitigating public concern, by providing the maximum seismic magnitude that could occur.

The relationship between seismic and aseismic fault-slip during fluid injection remains poorly understood.[32,60] Chen and Lapusta[51] modelled repeating earthquakes using a representative rate and state friction model and found that there was significant aseismic fault-slip ranging from more than 99% of total slip for the smallest repeating seismicity

produced in their model (with moment magnitude of approximately 0.3) to 20% of total slip for the largest repeating seismic events that they simulated (with moment magnitude 3.7). They used a creeping fault layer with velocity of 23 mm per year to activate seismicity, hence they did not consider fluid injection or its effect in their simulations. Lapusta and Liu[62] developed a three-dimensional method using the boundary integral method to simulate spontaneous seismic and aseismic fault-slip subject to slow tectonic loading. Their results showed that the widely used quasi-dynamic method produces much smaller slip velocities and rupture speeds during dynamic events compared to their fully dynamic simulations. They use a creeping fault layer with velocity of 32 mm per year to induce changes in the fault plane however, do not consider fluid
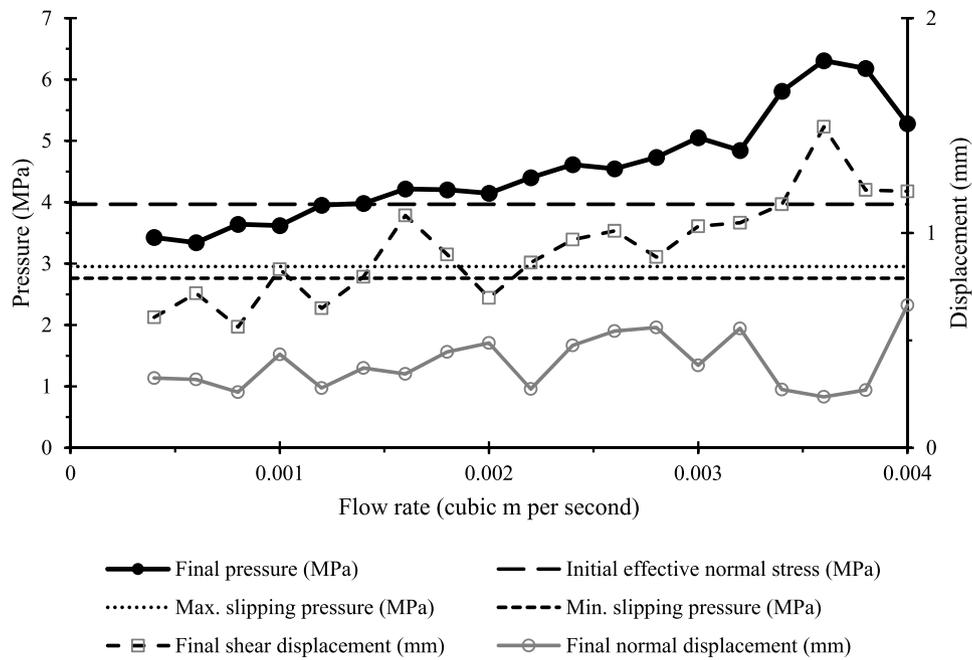
**Fig. 10.** Pressure, shear displacement and normal displacement at the injection point taken from the end of the simulation versus flow rates injecting 1 cubic m of water into the fault.
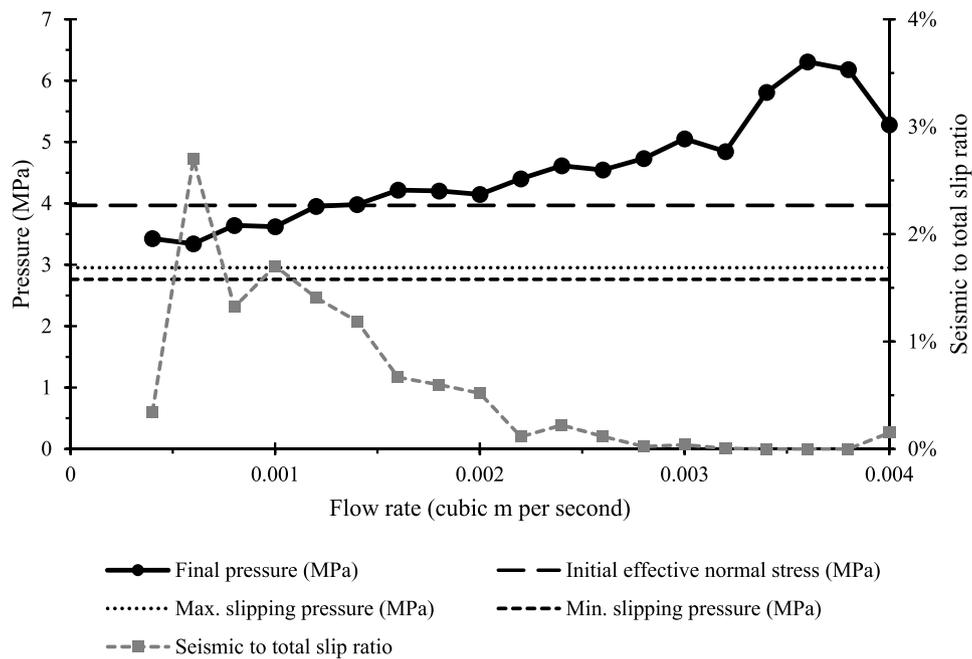


**Fig. 11.** Pressure at the injection point taken from the end of the simulation and seismic to total slip ratio versus flow rates injecting 1 cubic m of water into the fault.

effects or injection. Cappa et al.[29] used the Distinct Element Method (DEM)[63] via 3DEC[64] and show that fault-slip induced by fluid injection in a natural fault is quantitatively similar with fault-slip and frictional properties measured in the laboratory. They suggest that seismicity may be triggered indirectly by the fluid injection due to loading of the non-pressurised fault zones by aseismic slip. Their 3DEC model cannot consider fluid exchange between the fault and the rock mass and there were no inertial effects present. Wynants-Morel et al.[60] also used 3DEC to simulate fault-slip using synthetic case studies. They considered the

fault-slip seismic if the slip velocity is equal or greater to 1 mm/s; however, the simulation of seismic ruptures was quasi-dynamic, where an adaptive time stepping scheme was used, which is dependent on the unbalanced force ratio. In addition, they did not consider fluid transfer between the fault and the rock mass and did not compare their model to an in-situ experiment. In contrast, the method presented in this study is fully dynamic during the seismic slip, fluid transfer between the fault and the rock mass is accounted for, and an in-situ fluid injection experiment is used for the verification of the method whilst considering
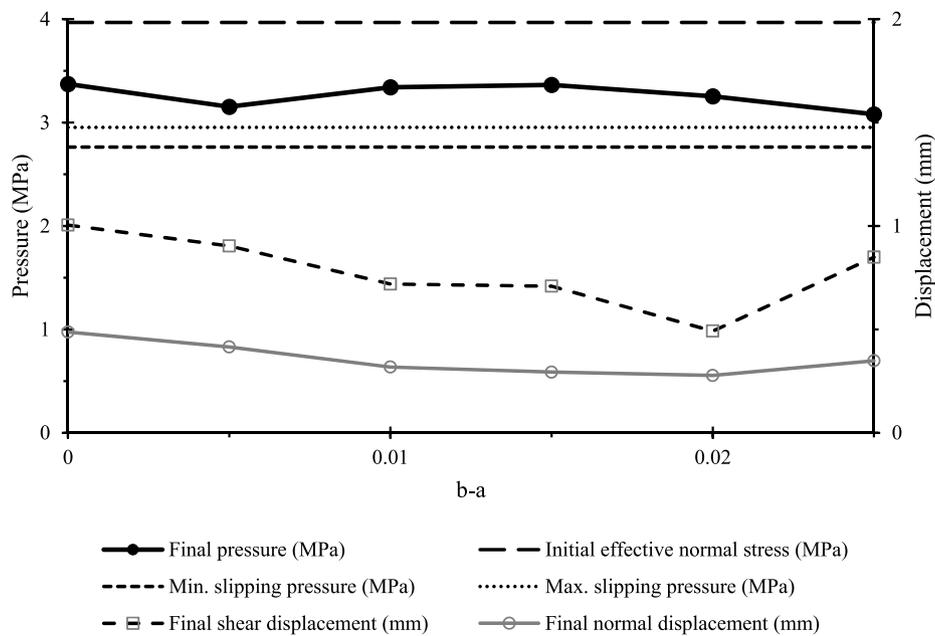
**Fig. 12.** Pressure, shear displacement and normal displacement at the injection point taken from the end of the simulation versus (*b–a*) values injecting 1 cubic m of water into the fault at a flow rate of $6 \times 10^{-4}$ cubic m per s.
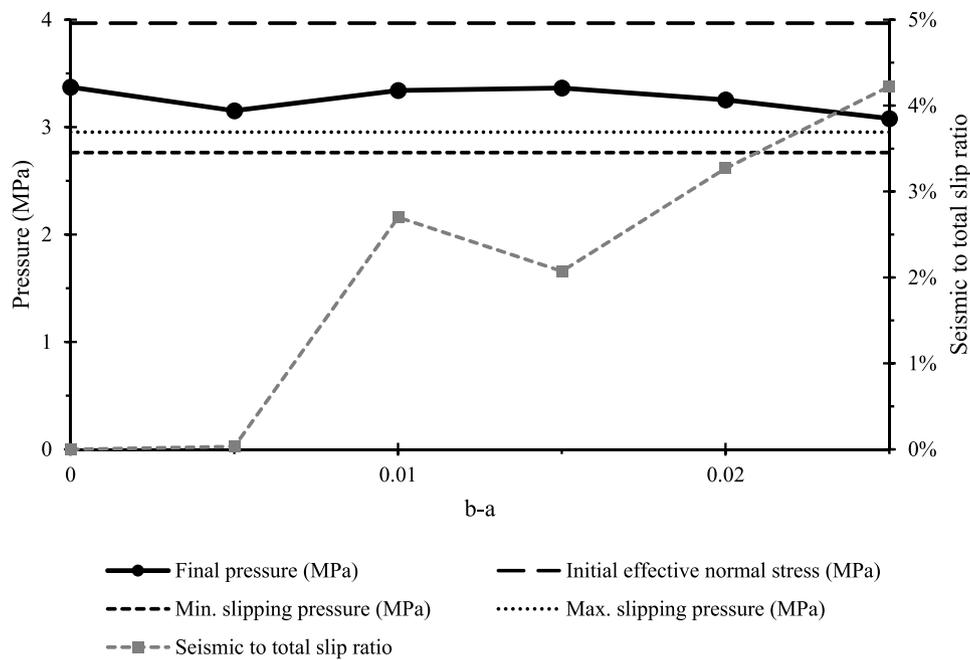


**Fig. 13.** Pressure at the injection point taken from the end of the simulation and seismic to total slip ratio versus (*b–a*) values injecting 1 cubic m of water into the fault at a flow rate of $6 \times 10^{-4}$ cubic m per s.

aseismic and seismic fault movements. Hence, the numerical simulation scheme developed in this study can be a reliable method to quantify fluid injection induced fault-slip in both quasi-static and dynamic conditions, although the code needs to be further extended to three dimensions for faults with complex geometries.

## 6. Conclusions

In this study a static and dynamic coupled X-FEM approach is presented to predict the pressure and movement of an in-situ experiment. By using history matching the simulated values produced became close to the measured data. The dynamic analysis was used when instability conditions were met, using a direct implication of rate and state friction. This calibrated model predicted the main seismic event and

corresponding magnitude that was recorded in the in-situ experiment. This result emphasises that under the in-situ experimental conditions that fault-slip was mainly aseismic, however <2% of the fault-slip was seismic. This illustrates the importance of considering and modelling the main mechanisms that contribute to fault-slip, including the fluid exchange between the rock mass and the fault core (approximated, in this case, by a through-going discontinuity). A parametric study investigating the injection rate (at a constant injection volume) indicated that seismicity may increase with injection rate then decrease when the fault becomes tensile. However, the higher injection rates may produce undesired tensile failure of the surrounding rock mass and/or cause fault propagation. By using the maximum seismic to total slip ratio the influence of the ($b$-$a$) value was investigated, illustrating with this method the amount of seismicity increases approximately linearly with the $b$ parameter. This demonstrates the importance of estimating or measuring important rock mass and fault properties before fluid injection takes place. By predicting the onset of seismicity and seismic magnitudes caused by fluid injection this would assist in determining fluid injection protocols for industry. Extension of this code to three-dimensional analysis could be considered. This may lead to a better understanding of seismicity from fluid injection, which could assist with mitigating the risks of injecting fluid underground.

## Declaration of competing interest

The authors declare that they have no known competing financial interests or personal relationships that could have appeared to influence the work reported in this paper.

## Acknowledgments

## References

1 Raleigh CB, Healy JH, Bredehoeft JD. An experiment in earthquake control at Rangely, Colorado. *Science*. 1976;191(4233):1230–1237. https://doi.org/10.1126/science.191.4233.1230.

2 Nicholson C, Wesson RL. Triggered earthquakes and deep well activities. *Pure Appl Geophys*. 1992;139(3):561–578. https://doi.org/10.1007/BF00879951.

3 Cornet FH, Helm J, Poitrenaud H, Etchecopar A. Seismic and aseismic slips induced by large-scale fluid injections. In: *Pure and Applied Geophysics*. Vol 150. Springer; 1997:563–583. https://doi.org/10.1007/s000240050093.

4 Majer EL, Baria R, Stark M, et al. Induced seismicity associated with enhanced geothermal systems. *Geothermics*. 2007;36(3):185–222. https://doi.org/10.1016/j.geothermics.2007.03.003.

5 Ellsworth WL. Injection-induced earthquakes. *Science*. 2013;341(6142). http://science.sciencemag.org/content/341/6142/1225942.abstract.

6 Sainoki A, Mitri HS. Dynamic behaviour of mining-induced fault slip. *Int J Rock Mech Min Sci*. 2014;66:19–29.

7 Sainoki A, Mitri HS. Dynamic modelling of fault-slip with Barton′s shear strength model. *Int J Rock Mech Min Sci*. 2014;67:155–163.

8 Sainoki A, Mitri HS. Effect of slip-weakening distance on selected seismic source parameters of mining-induced fault-slip. *Int J Rock Mech Min Sci*. 2015;73:115–122.

9 Aagaard BT, Knepley MG, Williams CA. A domain decomposition approach to implementing fault slip in finite-element models of quasi-static and dynamic crustal deformation. *J Geophys Res Solid Earth*. 2013;118(6):3059–3079.

10 Jin L, Zoback MD. Fully coupled nonlinear fluid flow and poroelasticity in arbitrarily fractured porous media: a hybrid-dimensional computational model. *J Geophys Res Solid Earth*. 2017;122(10):7626–7658.

11 Rutqvist J, Rinaldi AP, Cappa F, Moridis GJ. Modeling of fault reactivation and induced seismicity during hydraulic fracturing of shale-gas reservoirs. *J Petrol Sci Eng*. 2013;107:31–44. https://doi.org/10.1016/J.PETROL.2013.04.023.

12 Rutqvist J, Rinaldi AP, Cappa F, Moridis GJ. Modeling of fault activation and seismicity by injection directly into a fault zone associated with hydraulic fracturing of shale-gas reservoirs. *J Petrol Sci Eng*. 2015;127:377–386. https://doi.org/10.1016/J.PETROL.2015.01.019.

13 Rutqvist J, Wu Y-S, Tsang C-F, Bodvarsson G. A modeling approach for analysis of coupled multiphase fluid flow, heat transfer, and deformation in fractured porous rock. *Int J Rock Mech Min Sci*. 2002;39(4):429–442. https://doi.org/10.1016/S1365-1609(02)00022-9.

14 Jin L, Zoback MD. Fully dynamic spontaneous rupture due to quasi-static pore pressure and poroelastic effects: an implicit nonlinear computational model of fluid-induced seismic events. *J Geophys Res Solid Earth*. 2018;123(11):9430–9468.

15 Barton N. Review of a new shear-strength criterion for rock joints. *Eng Geol*. 1973;7(4):287–332.

16 Pruess K, Oldenburg CM, Moridis GJ. *TOUGH2 User's Guide Version 2. Published Online*. 1999.

17 Guglielmi Y, Cappa F, Avouac J-P, Henry P, Elsworth D. Seismicity triggered by fluid injection–induced aseismic slip. *Science*. 2015;348(6240):1224. LP - 1226 http://science.sciencemag.org/content/348/6240/1224.abstract.

18 Streit JE, Hillis RR. Estimating fault stability and sustainable fluid pressures for underground storage of CO2 in porous rock. *Energy*. 2004;29(9):1445–1456. https://doi.org/10.1016/j.energy.2004.03.078.

19 Rutqvist J, Birkholzer J, Cappa F, Tsang C-F. Estimating maximum sustainable injection pressure during geological sequestration of CO2 using coupled fluid flow and geomechanical fault-slip analysis. *Energy Convers Manag*. 2007;48(6):1798–1807. https://doi.org/10.1016/j.enconman.2007.01.021.

20 Moeck I, Kwiatek G, Zimmermann G. Slip tendency analysis, fault reactivation potential and induced seismicity in a deep geothermal reservoir. *J Struct Geol*. 2009;31(10):1174–1182. https://doi.org/10.1016/J.JSG.2009.06.012.

21 Cuss RJ, Harrington JF. An experimental study of the potential for fault reactivation during changes in gas and pore-water pressure. *Int J Greenh Gas Control*. 2016;53:41–55. https://doi.org/10.1016/j.ijggc.2016.07.028.

22 Wiseall AC, Cuss RJ, Hough E, Kemp SJ. The role of fault gouge properties on fault reactivation during hydraulic stimulation; an experimental study using analogue faults. *J Nat Gas Sci Eng*. 2018;59:21–34.

23 Schwartzkopff AK, Sainoki A, Elsworth D. Numerical simulation of an in-situ fluid injection experiment into a fault using coupled X-FEM analysis. *Rock Mech Rock Eng. Published online November*. 2020;27. https://doi.org/10.1007/s00603-020-02301-1.

24 Scholz CH. Earthquakes and friction laws. *Nature*. 1998;391(6662):37–42.

25 Scotti O, Cornet FH. In situ evidence for fluid-induced aseismic slip events along fault zones. In: *International Journal of Rock Mechanics and Mining Sciences and Geomechanics Abstracts*. Vol 31. Oxford; New York: Pergamon Press, 1974-c1996; 1994:347–358.

26 McGarr A. Maximum magnitude earthquakes induced by fluid injection. *J Geophys Res solid earth*. 2014;119(2):1008–1019.

27 Marone C. Laboratory-derived friction laws and their application to seismic faulting. *Annu Rev Earth Planet Sci*. 1998;26(1):643–696.

28 Scuderi MM, Collettini C. The role of fluid pressure in induced vs. triggered seismicity: insights from rock deformation experiments on carbonates. *Sci Rep*. 2016;6(1):1–9.

29 Cappa F, Scuderi MM, Collettini C, Guglielmi Y, Avouac J-P. Stabilization of fault slip by fluid injection in the laboratory and in situ. *Sci Adv*. 2019;5(3), eaau4065.

30 Linker MF, Dieterich JH. Effects of variable normal stress on rock friction: observations and constitutive equations. *J Geophys Res Solid Earth*. 1992;97(B4):4923–4940.

31 Scuderi MM, Collettini C, Marone C. Frictional stability and earthquake triggering during fluid pressure stimulation of an experimental fault. *Earth Planet Sci Lett*. 2017;477:84–96.

32 Avouac J-P. From geodetic imaging of seismic and aseismic fault slip to dynamic modeling of the seismic cycle. *Annu Rev Earth Planet Sci*. 2015;43:233–271.

33 Mohammadnejad T, Khoei AR. An extended finite element method for hydraulic fracture propagation in deformable porous media with the cohesive crack model. *Finite Elem Anal Des*. 2013;73:77–95.

34 Khoei AR, Vahab M, Hirmand M. An enriched–FEM technique for numerical simulation of interacting discontinuities in naturally fractured porous media. *Comput Methods Appl Mech Eng*. 2018;331:197–231. https://doi.org/10.1016/j.cma.2017.11.016.

35 Pan P-Z, Rutqvist J, Feng X-T, Yan F. Modeling of caprock discontinuous fracturing during CO2 injection into a deep brine aquifer. *Int J Greenh Gas Control*. 2013;19:559–575. https://doi.org/10.1016/J.IJGGC.2013.10.016.

36 Réthoré J, Borst R de, Abellan M. A two-scale approach for fluid flow in fractured porous media. *Int J Numer Methods Eng*. 2007;71(7):780–800.

37 De Borst R, Réthoré J, Abellan M-A. A numerical approach for arbitrary cracks in a fluid-saturated medium. *Arch Appl Mech*. 2006;75(10):595–606.

38 Khoei AR, Vahab M, Haghighat E, Moallemi S. A mesh-independent finite element formulation for modeling crack growth in saturated porous media based on an enriched-FEM technique. *Int J Fract*. 2014;188(1):79–108.

39 Khoei AR. *Extended Finite Element Method: Theory and Applications*. John Wiley & Sons; 2014.

40 Giner E, Sukumar N, Tarancón JE, Fuenmayor FJ. An Abaqus implementation of the extended finite element method. *Eng Fract Mech*. 2009;76(3):347–368. https://doi.org/10.1016/J.ENGFRACMECH.2008.10.015.

41 Kontoe S, Zdravkovic L, Potts DM, Menkiti CO. On the relative merits of simple and advanced constitutive models in dynamic analysis of tunnels. *Geotechnique*. 2011;61(10):815–829.

42 *ABAQUS. V6.14, Online Documentation Help, Theory Manual: Dassault Systms. Published Online*. 2016.

43 Renshaw CE. On the relationship between mechanical and hydraulic apertures in rough-walled fractures. *J Geophys Res Solid Earth*. 1995;100(B12):24629–24636.

44 Dieterich JH. Modeling of rock friction: 1. Experimental results and constitutive equations. *J Geophys Res Solid Earth*. 1979;84(B5):2161–2168.

45 Cappa F, Guglielmi Y, Rutqvist J, Tsang C-F, Thoraval A. Hydromechanical modelling of pulse tests that measure fluid pressure and fracture normal displacement at the Coaraze Laboratory site, France. *Int J Rock Mech Min Sci*. 2006;43(7):1062–1082.

46 Guglielmi Y, Cappa F, Amitrano D. High-definition analysis of fluid-induced seismicity related to the mesoscale hydromechanical properties of a fault zone. *Geophys Res Lett.* 2008;35(6).

47 Eftekhari M, Baghbanan A, Bagherpour R. The effect of fracture patterns on penetration rate of TBM in fractured rock mass using probabilistic numerical approach. *Arab J Geosci.* 2014;7(12):5321–5331.

48 Konstantinovskaya E, Rutqvist J, Malo M. CO2 storage and potential fault instability in the St. Lawrence Lowlands sedimentary basin (Quebec, Canada): insights from coupled reservoir-geomechanical modeling. *Int J Greenh Gas Control.* 2014;22: 88–110.

49 Oliver DS, Chen Y. Recent progress on reservoir history matching: a review. *Comput Geosci.* 2011;15(1):185–221. https://doi.org/10.1007/s10596-010-9194-2.

50 Moré JJ. The Levenberg-Marquardt algorithm: implementation and theory. In: *Numerical Analysis.* Springer; 1978:105–116.

51 Chen T, Lapusta N. Scaling of small repeating earthquakes explained by interaction of seismic and aseismic slip in a rate and state fault model. *J Geophys Res Solid Earth.* 2009;114(B1).

52 De Barros L, Cappa F, Guglielmi Y, Duboeuf L, Grasso J-R. Energy of injection-induced seismicity predicted from in-situ experiments. *Sci Rep.* 2019;9(1):1–11.

53 De Barros L, Guglielmi Y, Rivet D, Cappa F, Duboeuf L. Seismicity and fault aseismic deformation caused by fluid injection in decametric in-situ experiments. *Compt Rendus Geosci.* 2018;350(8):464–475.

54 De Barros L, Daniel G, Guglielmi Y, et al. Fault structure, stress, or pressure control of the seismicity in shale? Insights from a controlled experiment of fluid-induced fault reactivation. *J Geophys Res Solid Earth.* 2016;121(6):4506–4522.

55 Duboeuf L, De Barros L, Cappa F, Guglielmi Y, Deschamps A, Seguy S. Aseismic motions drive a sparse seismicity during fluid injections into a fractured zone in a carbonate reservoir. *J Geophys Res Solid Earth.* 2017;122(10):8285–8304.

56 Goodfellow SD, Nasseri MHB, Maxwell SC, Young RP. Hydraulic fracture energy budget: insights from the laboratory. *Geophys Res Lett.* 2015;42(9):3179–3187.

57 Calò M, Dorbath C, Cornet FH, Cuenot N. Large-scale aseismic motion identified through 4-DP-wave tomography. *Geophys J Int.* 2011;186(3):1295–1314.

58 Schmittbuhl J, Lengliné O, Cornet F, Cuenot N, Genter A. Induced seismicity in EGS reservoir: the creep route. *Geoth Energy.* 2014;2(1):1–13.

59 Hanks TC, Kanamori H. A moment magnitude scale. *J Geophys Res Solid Earth.* 1979; 84(B5):2348–2350.

60 Wynants-Morel N, Cappa F, De Barros L, Ampuero J. Stress perturbation from aseismic slip drives the seismic front during fluid injection in a permeable fault. *J Geophys Res Solid Earth.* 2020;125(7), e2019JB019179.

61 Preuss S, Herrendörfer R, Gerya T, Ampuero J, van Dinther Y. Seismic and aseismic fault growth lead to different fault orientations. *J Geophys Res Solid Earth.* 2019;124 (8):8867–8889.

62 Lapusta N, Liu Y. Three-dimensional boundary integral modeling of spontaneous earthquake sequences and aseismic slip. *J Geophys Res Solid Earth.* 2009;114(B9).

63 Cundall PA. Formulation of a three-dimensional distinct element model—Part I. A scheme to detect and represent contacts in a system composed of many polyhedral blocks. In: *International Journal of Rock Mechanics and Mining Sciences & Geomechanics Abstracts.* Vol 25. Elsevier; 1988:107–116.

64 Itasca Consulting Group Inc. *3DEC—Three-dimensional Distinct Element Code.* Published online. 2016.